HHS Public Access

Author manuscript

Free Radic Biol Med. Author manuscript; available in PMC 2016 April 14.

Published in final edited form as:

Free Radic Biol Med. 2012 November 1; 53(9): 1675–1679. doi:10.1016/j.freeradbiomed.2012.07.014.

Does iron inhibit calcification during atherosclerosis?

Reshmi Rajendran[a], **Ren Minqin**[a], **John A. Ronald**[b], **Brian K. Rutt**[b], **Barry Halliwell**[c], and **Frank Watt**[a,*]

[a]Centre for Ion Beam Applications, Department of Physics, National University of Singapore, Singapore 117542

[b]Robarts Research Institute, London, ON, Canada

[c]Department of Biochemistry, National University of Singapore, Singapore 117542

Abstract

Oxidative stress has been implicated in the etiology of atherosclerosis and even held responsible for plaque calcification. Transition metals such as iron aggravate oxidative stress. To understand the relation between calcium and iron in atherosclerotic lesions, a sensitive technique is required that is quantitatively accurate and avoids isolation of plaques or staining/fixing tissue, because these processes introduce contaminants and redistribute elements within the tissue. In this study, the three ion-beam techniques of scanning transmission ion microscopy, Rutherford backscattering spectrometry, and particle-induced X-ray emission have been combined in conjunction with a high-energy (MeV) proton microprobe to map the spatial distribution of the elements and quantify them simultaneously in atherosclerotic rabbit arteries. The results show that iron and calcium within the atherosclerotic lesions exhibit a highly significant spatial inverse correlation. It may be that iron accelerates the progression of atherosclerotic lesion development, but suppresses calcification. Alternatively, calcification could be a defense mechanism against atherosclerotic progression by excluding iron.

Keywords

Atherosclerosis; Iron; Calcium; PIXE; STIM; RBS; Free radicals

Introduction

Atherosclerosis is a progressive disease characterized by the accumulation of lipids, fibrous elements, inflammatory cells, and molecules as plaques within the arterial wall of medium and large arteries, thereby leading to narrowing of the vessel lumen. Oxidation of low-density lipoproteins (LDL) within the artery wall has been postulated to be an important step in disease development. Evidence has been produced for a number of species and methods by which LDL can be oxidized, metal ion-mediated oxygen radical formation being one of them [1]. Transition metals such as iron can catalyze the generation of highly reactive oxygen derived species such as hydroxyl radical ($OH^{\bullet}$) [2], which increase oxidative stress

*Corresponding author. phywattf@nus.edu.sg (F.Watt).

and can lead to the oxidation of LDL, promoting its subsequent unregulated uptake by macrophages and exacerbating disease development.

Reactive oxygen species also contribute to several complex structural and functional changes within the vessel wall [3] and vascular calcification has been postulated to be one of them. Oxidative stress has been shown to enhance the osteoblastic differentiation of vascular cells leading to calcium deposition [4]. It has also been suggested that hydrogen peroxide promotes a phenotypic switch of vascular smooth muscle cells from contractile to osteogenic phenotypes [5]. Studies also show that antioxidants can decrease the onset and degree of calcification [6]. Does this imply that metal (especially iron)-mediated oxidative stress can directly or indirectly affect vascular calcification?

To assess the relationship, if any, between calcium and iron, it is necessary to examine advanced atherosclerotic lesions, in which calcification is most often seen, using a technique that can spatially map iron and calcium simultaneously within lesions. The technique should also exhibit sufficiently high resolution and be able to quantify calcium and iron with adequate sensitivity without recourse to conventional fixing and staining, because these processes are known to cause trace element redistribution and contamination.

Microprobe techniques are most suitable for assessing morphological and elemental alteration in tissue. Here, the application of nuclear microscopy to map and quantify the elemental distribution within atherosclerotic lesions is described using a rabbit model. Rabbits fed a high-cholesterol diet rapidly and reproducibly develop advanced atherosclerosis [7,8]. Nuclear microscopy is a set of imaging techniques composed of scanning transmission ion microscopy (STIM), particle-induced X-ray emission (PIXE), and Rutherford backscattering (RBS) used in conjunction with a mega-electron-volt proton microprobe [8]. Using STIM for structural identification, RBS for matrix characterization, and PIXE for trace element analysis, it is possible to image and quantify elemental distribution in unstained sections of atherosclerotic tissue from the aortas of high-cholesterol-fed rabbits.

Materials and methods

Rabbit model

Because it is known that rabbits that are fed a high-cholesterol diet (0.15–0.3% w/w) over extended periods of time, and without the additional use of balloon injury or genetic modifications, develop lesions that resemble late-stage atherosclerotic lesions [7–11], this model was chosen for this study. Aorta samples were obtained from three male New Zealand White rabbits. Two of the rabbits were fed a 0.25% w/w cholesterol diet for 8 months followed by 0.125% w/w cholesterol diet for another 10 months, and the third rabbit was fed the 0.25% diet for 17 months followed by the 0.125% diet for an additional year. Previous nuclear microscopy experiments carried out at the Centre for Ion Beam Applications (CIBA) over the past decade have shown that once atherosclerosis sets in, the elemental distribution exhibits similar trends regardless of age or the duration of cholesterol feeding [8]. Because the focus of the study was on examining the spatial distribution and relationship between iron and calcium, the variations in age and duration of administration of high-cholesterol

diet were not considered a limitation. In addition, it was also found that lesion development and calcification vary both around the artery wall and along the artery.

Experimental details

Ten-micrometer sections of unfixed and unstained tissue were collected on pioloform-wrapped aluminum nuclear microscopy holders. Nuclear microscopy experiments were carried out at the CIBA The instrumentation consists of a high-brightness High Voltage Engineering Europa 3.5-MeV Singletron ion accelerator, connected to three state-of-the-art beam lines. The nuclear microscope beam-line facility incorporates an Oxford Microbeams OM2000 end station with the OM50 quadrupole lenses configured in the high-excitation triplet mode. The principles behind the three nuclear microscopy techniques used are briefly described below.

PIXE

When a fast-moving proton of mega-electron-volt energy knocks out an electron from an inner shell, the vacancy is filled by an electron from the outer shell. This is accompanied by the emission of an X-ray quantum with energy equal to the difference in energy between these two levels. The energy of this X-ray being characteristic of the parent atom, this method can be used to determine the elements in a sample. X-rays of various elements are detected simultaneously using a lithium-drifted silicon X-ray detector placed at 90° to the beam axis and fitted with a filter designed for detection of elements above sodium in the periodic table. Iron and calcium were mapped based on the Kα line at 6.4 keV and the Kβ line at 4.01 keV, respectively. The Kβ line was chosen over the Kα line at 3.7 keV to prevent interference from the nearby Kβ line of potassium at 3.6 keV. The quantification in PIXE was validated by the use of a standard target of known elemental composition with certified homogeneity, manufactured by the National Institute of Standards and Technology (USA).

RBS

There is a lower, but significant probability that the interacting proton collides with the nucleus of the atom, in which case it can be backscattered and detected by a silicon surface barrier detector. The energy of the backscattered proton contains information on the mass of the target nucleus as well as its depth in the specimen, thereby giving information on the thickness and the matrix composition. In biological tissue, the density and composition of the major matrix elements carbon and oxygen can be estimated by measuring the energy and number of the back-scattered protons. Because the biological matrix is composed of light elements, nuclear reactions can take place, and therefore non-Rutherford cross sections were taken into account [12]. In addition, the energy of the proton beam was also chosen to be 2.1 MeV to avoid a sharp nuclear resonance for carbon at 1.7 MeV.

STIM

This technique relies on the well-defined energy loss of a high-energy ion, caused by ion-electron interactions, as it passes through organic samples with thicknesses of 30 μm or less. Because of the large momentum differences between the ion and the electron, the ion-electron interaction scattering angles are small, and the probability of large-angle scattering

from nuclear interactions is negligible [13]. Therefore the ion beam suffers only minimal spreading when it passes through the sample and this makes imaging of fine details possible in relatively thick sections. Off-axis STIM rather than low-current direct STIM was employed so as to make it compatible with the beam currents suitable for simultaneous PIXE and RBS measurements. During the experiments, off-axis STIM, RBS, and PIXE were simultaneously applied to increase the efficiency of data collection.

Quantitative measurements

The PIXE X-ray and RBS energy spectra were obtained from regions of interest (ROI) based on the structural information obtained from the STIM maps. The data obtained from RBS allowed quantification of light matrix elements such as C, N, and 0. Fitting the RBS spectra using SIMNRA [14] software in conjunction with Dan32 software allowed for integrated charge correction, thus enabling quantitative data pertaining to the elemental concentrations down to the parts per million of the ROI to be extracted from the PIXE spectra by Dan32 [15]. Other software codes such as Gupix and Mathematica were also employed to assist in elemental quantification. The correlation graphs were generated from the elemental maps of calcium and iron using OM-DAQ and Origin Pro 8.0. The elemental maps of calcium and iron were overlain using Adobe Photoshop to illustrate spatial anti-correlation.

For statistical analysis, the correlation coefficient, r, and the significance were calculated based on the correlation analysis using the data analysis package provided by Excel and statistical tables [16]. Differences were considered significant when a confidence interval of 99.9% was exceeded ($p < 0.001$).

Results

Structural and elemental mapping

Using a 2.1-MeV proton beam focused down to a spot size of 1 μm, large area scans were carried out to examine the structure of the tissue and the distribution of the elements across artery sections from rabbits with advanced atherosclerosis. The results were similar to earlier studies from the Centre for Ion Beam Applications, National University of Singapore, on rabbits with early lesions [8,17] with lesion size varying at different points around the artery wall and iron concentrations being significantly higher in the lesions compared to the underlying arterial wall. In addition, calcification was mainly found within the lesions at the lesion-artery wall interface, with similar-sized lesions exhibiting varying degrees of calcification. The present observations additionally show that areas with high iron levels inversely correlate with high calcium levels in all samples investigated (Fig. 1). Fig. 2 shows the results of a higher magnification scan over a representative artery section, indicating visually that there is a striking inverse correlation between the spatial distribution of iron and calcium and that this spatial anti-correlation is highly localized.

Quantitative analysis

Statistical analyses were carried out on calcium and iron levels to check the validity of the observed anti-correlation. In Fig. 3, the calcium and iron signals from a localized region that was selected based on the structural and elemental maps are plotted against distance along

the lesion and show an obvious anti-correlation ($r = -0.85$, $p < 0.001$). In Fig. 4 calcium and iron signals from a region encompassing both lesion and artery wall are plotted as a scatter plot. By dividing the elemental maps into 16 × 16 pixels, statistical analysis shows that the calcium and iron concentrations are strongly negatively correlated ($r = -0.75$), indicating a statistically significant ($p < 0.001$) degree of anti-correlation.

The elemental concentrations from all the arterial cross sections of all eight samples analyzed are listed in Table 1. The samples, all with significant lesion development, exhibit iron concentrations ranging from 24 to 87 ppm, with an average value of 63.5 ppm, and calcium concentrations ranging from 742 to 3150 ppm with an average value of 1882 ppm. These results show a weak (but not significant) degree of negative correlation ($r = -0.26$), which indicates that although there is a high degree of anti-correlation in the spatial distribution of calcium and iron within each section, average calcium and iron concentrations between sections do not exhibit significant anti-correlation. The calcium and iron concentrations showed no correspondence between samples compared at fixed distances from the heart or within the same rabbit at various distances from the heart.

Discussion

In this study, a statistically significant negative correlation in the spatial distributions of calcium and iron concentrations is observed within advanced atherosclerotic lesions in rabbits fed a high-cholesterol diet. In vitro studies and studies on genetic disorders have already suggested an inverse link between calcium and iron: in genetic hemochromatosis, increased iron was shown to decrease femoral neck bone mineral density, reduce plasma calcium, and elevate urinary excretion of calcium [18]. It has also been shown that sodium nitroprusside, used therapeutically as a vasodilating drug in heart transplantations, inhibits mineralization in a cell culture system by releasing iron ions. Addition of the iron chelator deferoxamine antagonizes this inhibiting effect [19].

Our previous investigations into the role of iron in atherosclerosis have shown that early lesions contain elevated concentrations of iron and identified a positive correlation between high iron levels and lesion development [17]. In addition, iron chelation therapy using desferrioxamine has been shown to slow down the early stages of atherosclerosis presumably by decreasing iron levels [20]. This early work supported the theory that iron ion-mediated oxygen radical formation contributes to lesion development and progression. Indeed, Saeed et al. [21] reported that lowering of macrophage iron increased expression of cholesterol export proteins in mature atherosclerotic lesions and decreased foam cell formation [21]. Because elevated iron levels precede calcium accumulation, our current results are consistent with the idea that elevated levels of localized iron can lead to the suppression of calcification. Indeed, in some tissues iron can enter cells via L-type Ca^{2+} channels [22], and Ca^{2+} channel blockers can reverse iron overload in liver [23]. It is not impossible that Fe^{2+} and Ca^{2+} compete for transport. The inverse relationship between iron and calcium concentrations in atherosclerotic plaques may be a reflection of contrasting distribution of ion accumulation in different cells or an alteration of cellular composition in the plaque over time. More information on the primary cellular localization of iron and calcium in the lesions is required to answer this question. We have therefore potentially an

interesting phenomenon, in that iron contributes to lesion development but suppresses calcification. An equally interesting alternative explanation, however, could be that calcification is a defense mechanism that protects against high accumulations of localized iron.

References

1. Fu S, Davies MJ, Stacker R, Dean RT. Evidence for roles of radicals in protein oxidation in advanced human atherosclerotic plaque. Biochem. J. 1998; 333:519–525. [PubMed: 9677308]
2. Halliwell, B.; Gutteridge, JMC., editors. Free Radicals in Biology and Medicine. 4th. London: Oxford University Press; 2007.
3. Chrissobolis S, Faraci FM. The role of oxidative stress and NADPH oxidase in cerebrovascular disease. Trends Mol. Med. 2008; 14:495–502. [PubMed: 18929509]
4. Mody N, Parhami F, Sarafin TA, Demer LL. Oxidative stress modulates osteoblastic differentiation of vascular and bone cells. Free Radic. Biol. Med. 2001; 31:509–519. [PubMed: 11498284]
5. Byon CH, Javed A, Dai Q, Kappes JC, Clemens TL, Darley-Usmar VM, McDonald JM, Chen Y. Oxidative stress induces vascular calcification through modulation of the osteogenic transcription factor Runx2 by AKT signalling. Biol. Chem. 2008; 283:15319–15327.
6. Tang FT, Chen SR, Wu XQ, Wang TQ, Chen JW, Li J, Bao LP, Huang HQ, Liu PQ. Hypercholesterolemia accelerates vascular calcification induced by excessive vitamin D via oxidative stress. Calcif. Tissue Int. 2006; 79:326–339. [PubMed: 17120185]
7. Daley SJ, Klemp KF, Guyton JR, Rogers KA. Cholesterol fed and casein fed rabbit models of atherosclerosis. Part 2. Differing morphological severity of atherogenesis despite matched plasma cholesterol levels. Arterioscler. Thromb. 1994; 14:105–141. [PubMed: 8274465]
8. Watt F, Rajendran R, Ren MQ, Tan BKH, Halliwell B. A nuclear microscopy study of trace elements Ca, Fe, Zn and Cu in atherosclerosis. Mid. Instrum. Methods Phys. Res. B. 2006; 249:646–662.
9. Adams CW, Miller N, Morgan RS, Rao SN. Lipoprotein levels and tissue lipids in fatty-fibrous atherosclerosis induced in rabbits by two years cholesterol feeding at a low level. Atherosclerosis. 1982; 44:1–8. [PubMed: 7115472]
10. Ronald JA, Walcarius MSR, Robinson JF, Hegele RA, Rutt BK, Rogers KA. MRI of early and late stage arterial remodelling in a low level cholesterol-fed rabbit model of atherosclerosis. J. Magn. Reson. Imaging. 2007; 26:1010–1019. [PubMed: 17896368]
11. Finking G, Hanke H. Nikolaj Nikolajewitsch Anitschkow (1885–1964) established the cholesterol-fed rabbit as a model for atherosclerosis research. Atherosclerosis. 1997; 135:1–7. [PubMed: 9395267]
12. Doolittle LR. A semiautomatic algorithm for Rutherford backscattering analysis. Nucl. Instrum. Methods Phys. Res. B. 1986; 15:227–231.
13. Johansson, SAE.; Campbell, JL.; Malmqvist, KG., editors. Particle Induced X-ray Emission Spectrometry (PIXE). London: Wiley; 1995.
14. Mayer, M. SIMNRA Users Guide Technical Report IPP 9/113. Garching, Germany: Max-Planck-Insitut fur Plasmaphysik; 1996.
15. Maxwell JA, Campbell JL, Tesdale WJ. The Guelph PIXE software package. Nucl. Instrum. Methods Phys. Res. B. 1988; 43
16. Jerrold, HZ., editor. Biostatistical Analysis. Upper Saddle River, NJ: Prentice Hall; 1984.
17. Ren MQ, Watt F, Tan BKH, Halliwell B. Correlation of iron and zinc levels with lesion depth in newly formed atherosclerotic lesions. Free Radic. Biol. Med. 2003; 34:746–752. [PubMed: 12633751]
18. Kudo H, Suzuki S, Watanabe A, Kikuch H, Sassa S, Sakamoto S. Effects of colloidal iron overload on renal and hepatic siderosis and the femur in male rats. Toxicology. 2008; 246:143–147. [PubMed: 18289763]

19. Huitmea LF, van Weeren PR, Barneveld A, van de Lest CH, Helms JB, Vaandrager AB. Iron derived from the nitric oxide donor sodium nitro-prusside inhibits mineralization. Eur.J. Pharmacol. 2006; 542:48–53. [PubMed: 16828741]

20. Ren MQ, Rajendran R, Ning P, Tan BKH, Ong W-Y, Watt F, Halliwell B. The iron chelator desferioxamine inhibits atherosclerotic lesion development and decreases lesion iron concentrations in the cholesterol-fed rabbit. Free Radic. Biol. Med. 2005; 38:1206–1211. [PubMed: 15808418]

21. Saeed O, Otsuka F, Polavarapu R, Karmali V, Weiss D, Davis T, Rostad B, Pachura K, Adams L, Elliott J, Taylor WR, Narula J, Kolodgie E, Virmani R, Hong CC, Finn AV. Pharmacological suppression of hepddin increases macrophage cholesterol efflux and reduces foam cell formation and atherosclerosis. Arterioscler. Thromb. Vase. Biol. 2012; 32:299–307.

22. Oudit GY, Sun H, Trivieri MG, Koch SE, Dawood F, Ackerley C, Yazdanpanah M, Wilson GJ, Schwartz A, Liu PP, Backx PH. L-type Ca^{2+} channels provide a major pathway for iron entry into cardiomyocytes in iron-overload cardiomyopathy. Nat. Med. 2003; 9:1187–1194. [PubMed: 12937413]

23. Ludwiczek S, Theurl I, Muckenthaler MU, Jakab M, Mair SM, Theurl M, Kiss J, Paulmichl M, Hentze MW, Ritter M, Weiss G. Ca^{2+} channel blockers reverse iron overload by a new mechanism via divalent metal transporter-1. Nat. Med. 2007; 13:448–454. [PubMed: 17293870]

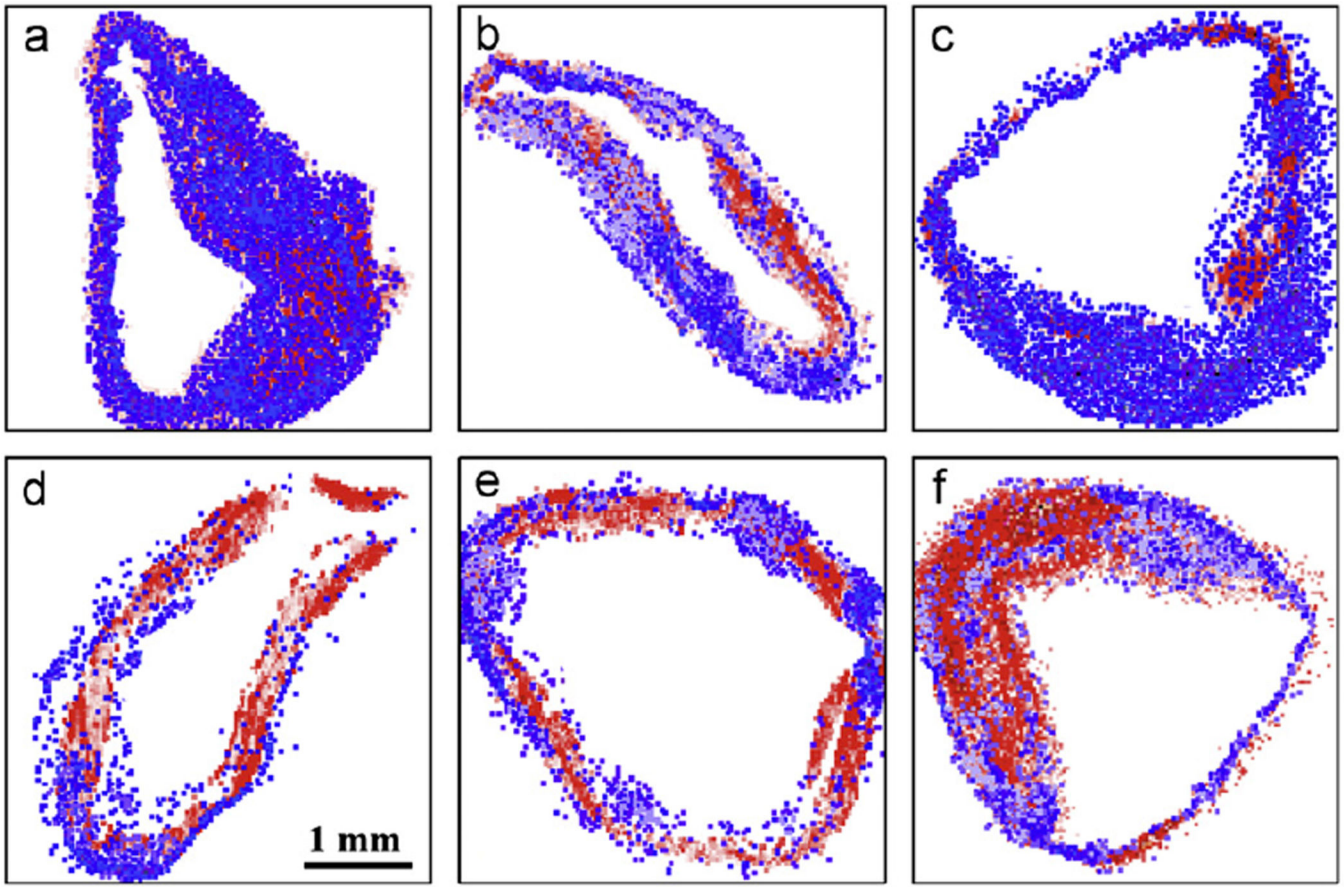

Fig. 1.

(a–f) Elemental map overlays of typical artery sections from rabbits with late-stage atherosclerosis. The calcium distribution is represented by red and the iron distribution by blue.

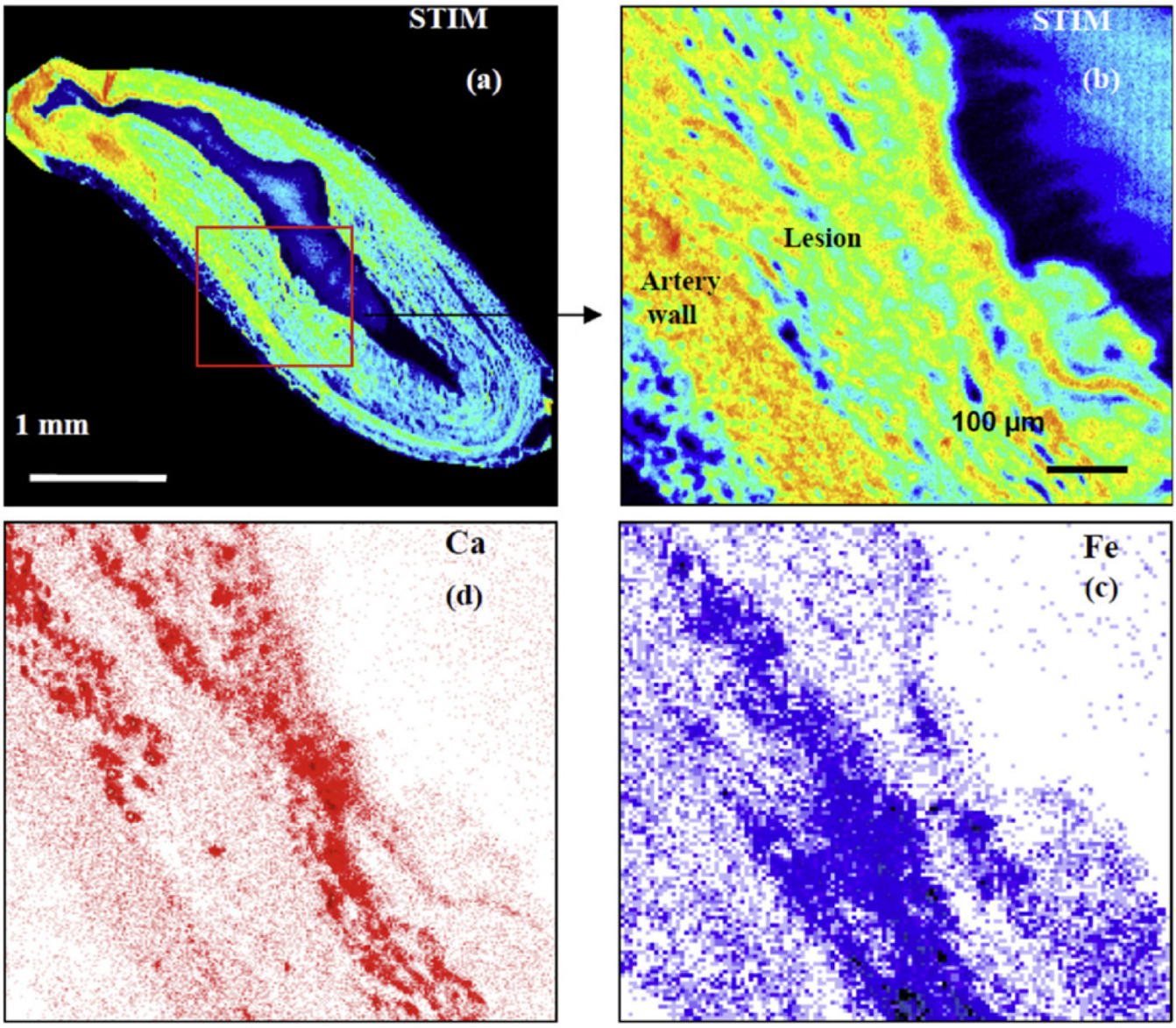

Fig. 2.

(a) STIM image of the artery section corresponding to the elemental map in Fig. 1b. (b) Higher magnification STIM image of the area depicted by the red box in (a), (c) Elemental map of iron and (d) elemental map of calcium from the same area.

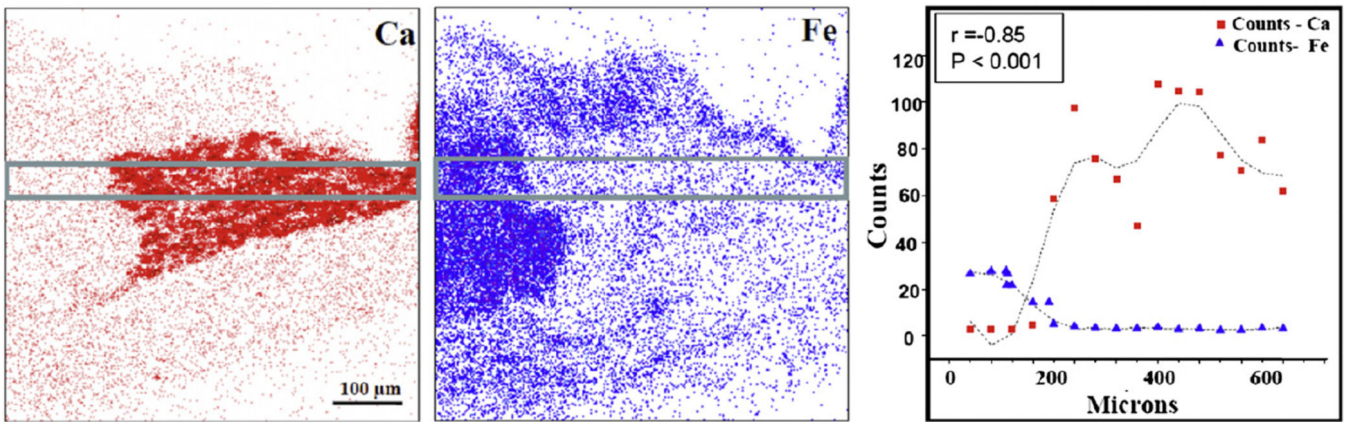

Fig. 3.

The calcium and iron elemental maps from a typical arterial tissue section and the graph showing the characteristic PIXE X-ray counts for calcium and iron plotted across the lesion as depicted by the area within the two parallel lines.

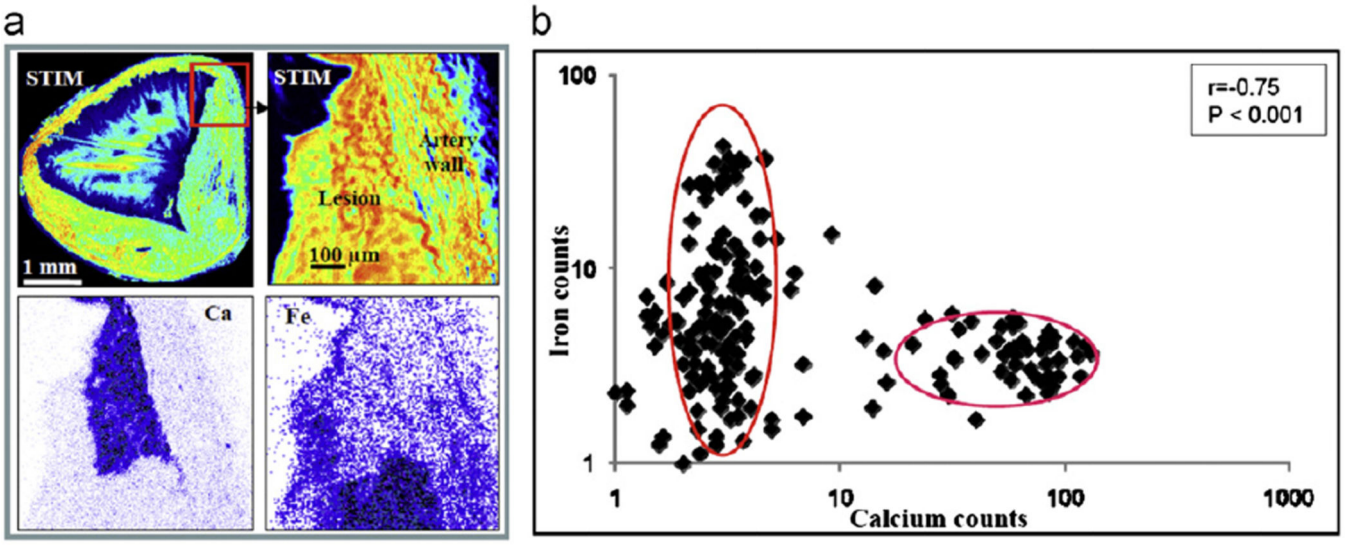

Fig. 4.

(a) Clockwise from top left—STIM image of the whole artery section as shown in Fig. 1c, STIM image, and iron map and calcium map from the area depicted by the red box. (b) Scatter plot showing calcium and iron PIXE characteristic X-ray counts. The counts are calculated by dividing the scanned region into 16 × 16 pixels and plotting the Ca count against the Fe count for each pixel (note the log plot). The pixels containing high calcium correspond to the pixels containing low iron.

Table 1

The elemental concentration in parts per million, with the error in parentheses, of the artery sections from the eight samples analyzed.

	Sample 1	Sample 2	Sample 3	Sample 4	Sample 5	Sample 6	Sample 7	Sample 8
P	2577.2 (69.2)	2042.2 (64.4)	2486.1 (77.3)	2693.1 (79.6)	2606.0 (78.3)	2367.0 (70.4)	3061.4 (85.8)	2849.7 (82.5)
S	373.8 (22.6)	1532.3 (62.2)	1652.4 (71.8)	1826.1 (56.9)	1551.7 (71.4)	1316.4 (62.3)	1910.3 (83.1)	1760.2 (59.6)
Cl	618.4 (22.4)	3088.9 (73.8)	4215.6 (94.8)	1757.5 (48.9)	3491.2 (88.3)	2954.7 (76.1)	4704.8 (107.1)	2225.4 (53.9)
K	1380.4 (27.9)	942.4 (25.3)	645.5 (24.7)	770.9 (25.9)	539.9 (28.5)	472.7 (24.9)	493.8 (28.3)	864.0 (25.7)
Ca	**1352.6 (18.9)**	**742.1 (14.9)**	**1525.7 (24.9)**	**1664.6 (25.2)**	**2824.5 (40.4)**	**2463.0 (35.8)**	**3149.9 (41.3)**	**1313.0 (20.9)**
Fe	**82.70 (1.2)**	**86.7 (2.1)**	**53.5 (1.6)**	**82.2 (1.9)**	**50.0 (1.7)**	**76.7 (2.0)**	**51.9 (1.6)**	**24.2 (1.1)**
Zn	17.4 (0.8)	12.7 (1.4)	12.3 (1.3)	27.8 (1.6)	15.5 (1.62)	10.8 (1.4)	14.4 (1.4)	20.5 (1.6)

Free Radic Biol Med. Author manuscript; available in PMC 2016 April 14.